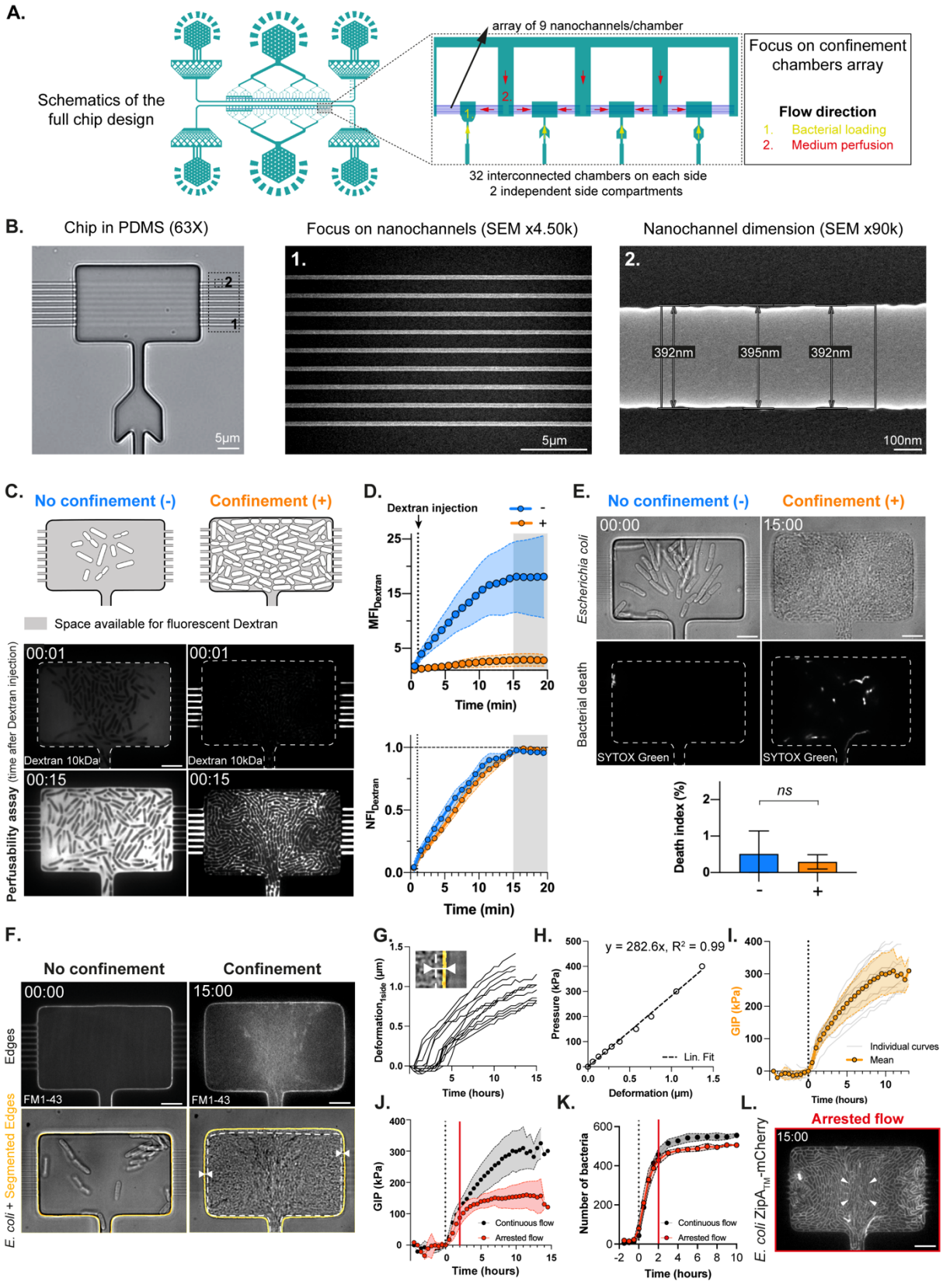

Supplementary Figure 1

Supplementary Figure 1:

A. Design of the microfluidic chip (*left*) and magnified view of one motif of the confinement-chambers array (*right*). The chip contains two independent sides comprising 32 chambers of various geometries. This study focuses on the 18 rectangular chambers shown in Figure 1.A. Arrows depict the flows applied during bacterial loading (yellow) and subsequent continuous medium perfusion (red). B. Brightfield image of the bacterial confiner (*left*) with two regions highlighted in insets, showing Scanning Electron Microscopy (SEM) images of the 400nm-wide nanochannel array (*middle*, Inset 1) and one single nanochannel for characterization of its dimensions (*right*, Inset 2). C. Schematics of Dextran-FITC (10 kDa) perfusability assays in the bacterial confiner without (*top left*, blue) and with confinement (*top right*, orange). Timelapse confocal images (1 minute frame intervals) showing Dextran perfusion before and 3.5 h after GIP build-up (*bottom*). Dextran was injected 1 min after acquisition started denoted as Time 0 (Supp. Video 1). D. Temporal evolution of Dextran fluorescence in the chamber, shown as mean (MFI, *top*) and normalized (NFI, *bottom*) fluorescence intensity before (blue, $n_{chambers} = 3$) and upon confinement (orange, $n_{chambers} = 2$). NFI is defined as the MFI divided by its maximum value reached within 15-20 minutes after Dextran injection (vertical dotted line), corresponding to the time needed to fill all the interstitial space. E. Bacterial viability using the DNA intercalant SYTOX Green. Brightfield and confocal images of SYTOX-stained bacteria without and with confinement (*top*). Quantification of the death index without ($n_{FOV} = 48$, $n_{chambers} = 9$) and with confinement ($n_{FOV} = 199$, $n_{chambers} = 10$) (*bottom*). The death index is defined as the percentage of the chamber surface positive to SYTOX Green, corresponding on average to 4-5 dead cells per chamber at late confinement. Significance was assessed using a Mann-Whitney test. F. Characterization of the mechanical environment. Confocal (*top*) and brightfield (*bottom*) images of bacteria growing in a chamber whose walls were stained with FM1-43, shown in without and with confinement (0 h and 15 h, *left* and *right*, resp.). Segmented chamber edges are highlighted in orange. The white arrow indicates the final chamber deformation respect to its initial size (white dashed line). G. Chamber deformation along the x-axis (inset) over time. Each curve corresponds to one single chamber (n = 13, N = 3) (Supp. Video 2). H. Calibration of PDMS deformability (Methods). Experimental data points were fitted with a linear regression curve (black dotted line). I. Quantification of GIP (n = 13, N = 3). Individual curves (grey) are inferred from individual deformations (Panel G), by using the calibration curve (Panel H) and rescaled to the time 0 of GIP build-up. J. Temporal evolution of GIP under constant perfusion (gray, shown in Panel I) and upon perfusion arrest (red) 2 hours after confinement onset, indicated by the red line. K. Temporal evolution of bacterial number under constant perfusion (gray, shown in Figure 1.D) and upon perfusion arrest (red) 2 hours after confinement onset, indicated by the red line. L. Representative image of confined bacteria getting largely squeezed without medium perfusion (white arrowheads, *bottom*). Mean values ± s.t.d. are represented. Time is indicated as hh:mm. Scale bars: 5 µm.

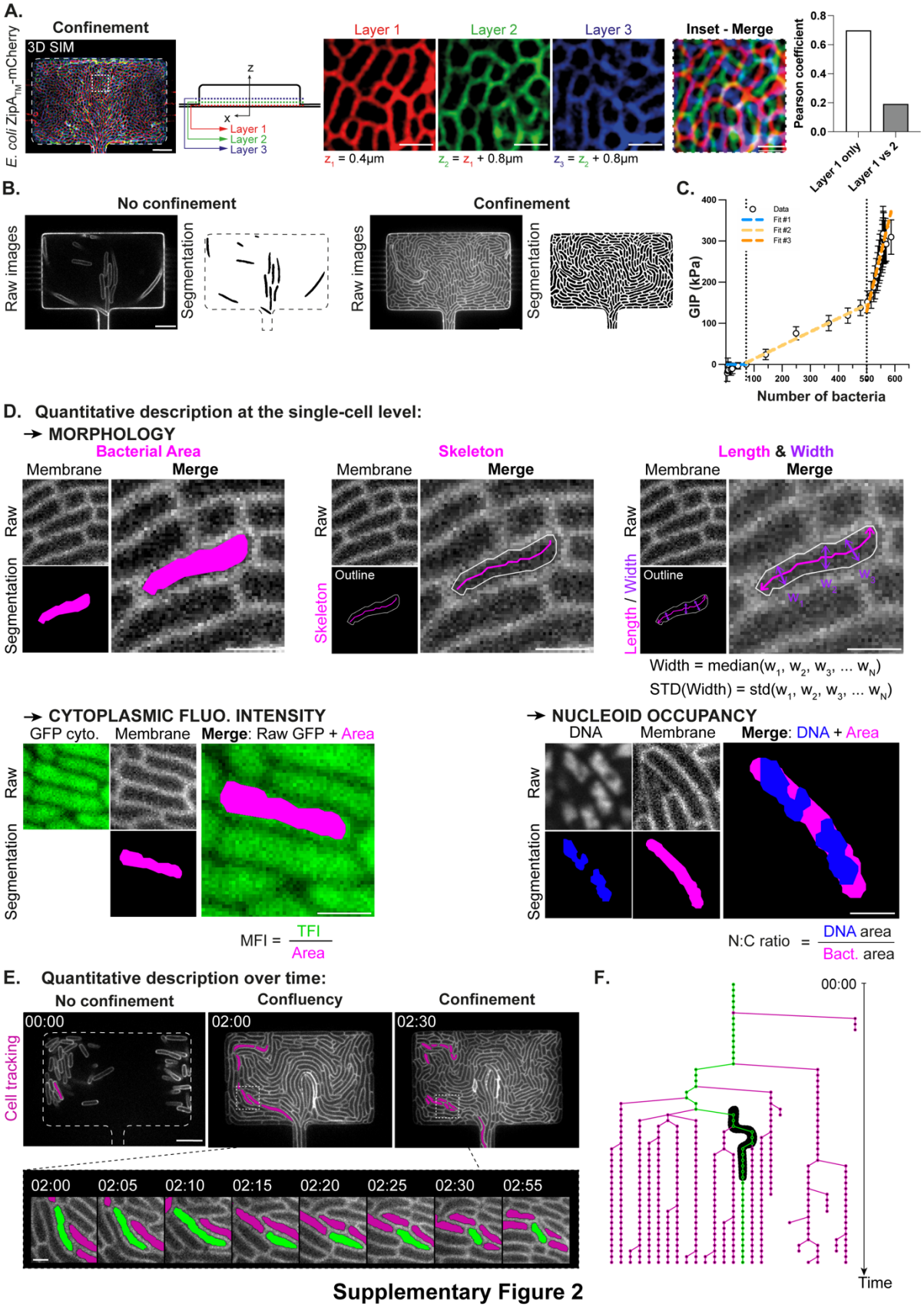

Supplementary Figure 2

Supplementary Figure 2:

A. 3D SIM super-resolution images of confined bacteria labelled at the inner membrane (*left*). Cross-sectional schematics of the three first bottom layers of bacteria, spaced 0.8 µm apart to match bacterial width (width = 0.82 $\pm$ 0.06µm, $n_{bacteria}$ = 10), and corresponding color-coded focal planes from the inset (white dashed line) to zoom-in on single bacteria (*center*). Pearson correlation indicates that bacteria in the focal plane (layer 1) are mostly not verticalized ($n_{chamber}$ = 1) (*right*). B. Confocal images of *E. coli* bacteria and corresponding segmentation in the absence and presence of confinement (*left* and *right* resp.) (Methods). C. Relationship between GIP and the number of bacteria (2D) with perfusion. We identified three regimes: (1) bacteria increase in number without generating GIP before confinement (Fit 1, blue: y = 0); (2) the number of bacteria and GIP increase rapidly (Fit 2, yellow: y = 0.3305 x - 19.74, R^2 = 0.9); (3) the number of bacteria increases slowly while the GIP continues to increase (Fit 3, orange: y = 2.796 x - 1269, R^2 = 0.5). D. Single-cell quantitative description of bacterial physiology under confinement. For each parameter, representative raw images with computed features (magenta) and merge are shown, with equations where applicable. Parameters include bacterial morphology (area, skeleton, length, width), cytoplasmic fluorescence, and nucleoid occupancy. (Supp. Video 3). E. Time-resolved quantitative description of bacterial physiological changes. Timelapse confocal images of proliferating *E. coli* bacteria labeled at the inner membrane in the bacterial confiner (*top*). Single-cell tracking (Methods) allows to follow bacterial generations with respect to the onset of confinement. One bacterial family is depicted in pink, a single bacterium (green) undergoes two cycles of division and shortens upon GIP build-up (*bottom*). Scale bar inset: 1µm (Supp. Video 3). F. Lineages of the bacterial family depicted in pink (Panel D). Points represent individual bacteria over time; lines connect the same bacterium across timepoints. Branching indicates division. The dark region refers to the time-resolved inset shown in Panel E. Scale bars 5 µm, unless otherwise stated.

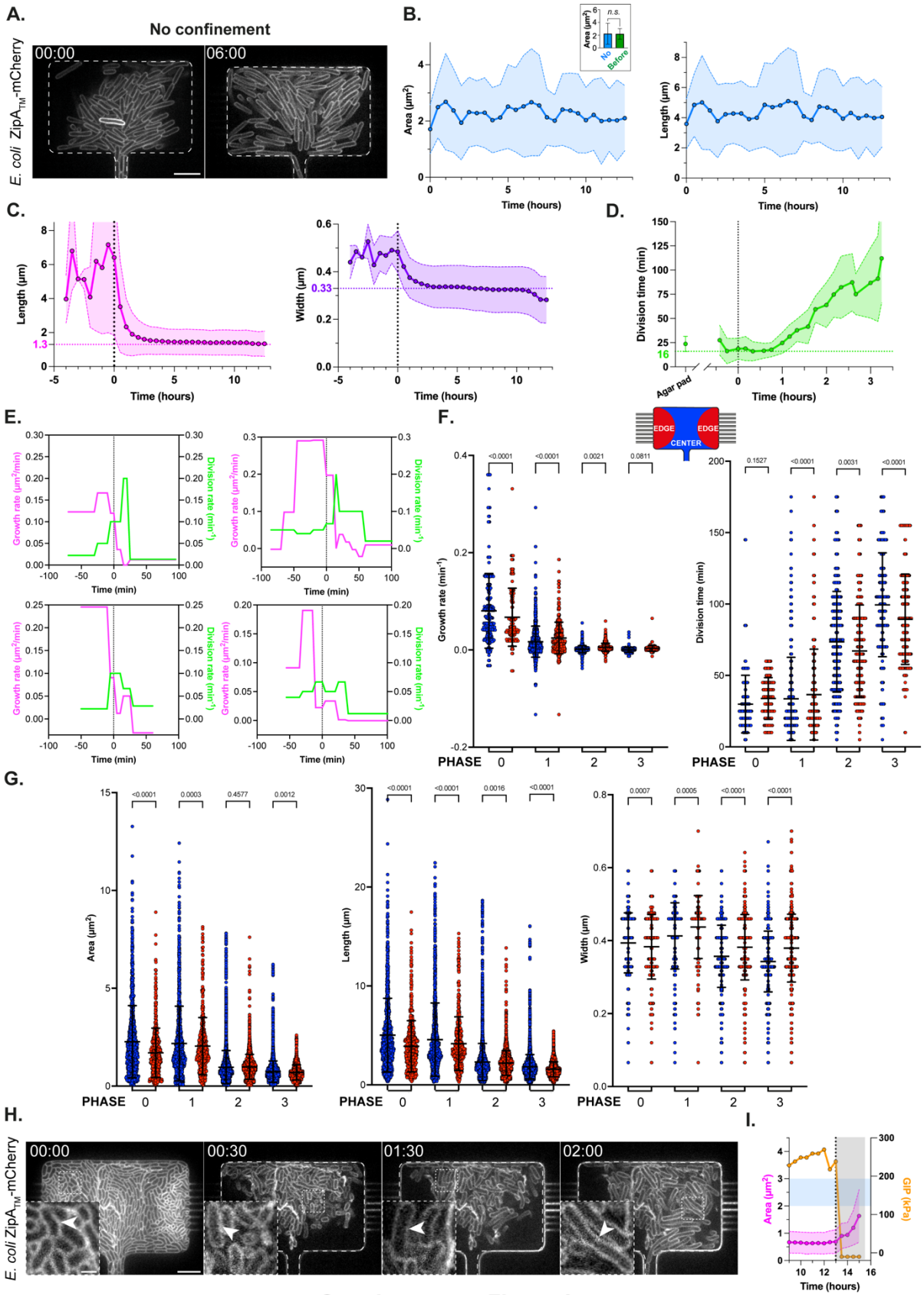

Supplementary Figure 3

Supplementary Figure 3:

A. Timelapse confocal images of proliferating bacteria labelled at the inner membrane (grey) in the absence of confinement. B. Quantification of bacterial area (*left*) and length (*right*) in the absence of confinement ($n_{bacteria}$ = 3871, $n_{chambers}$ = 1). The inset shows no statistical difference in bacterial area between the unconfined condition and before confinement (Figure 2.C), as assessed by one-way ANOVA. C. Bacterial length and width in the presence of confinement ($n_{bacteria}$ = 47834, $n_{chambers}$ = 4) corresponding to Figure 2.B. Final values reached at late stages of confinement are highlighted. D. Bacterial division time in agar pad during exponential growth phase (*left*, $n_{bacteria}$ = 526, n_{tracks} = 68) and upon confinement (*right*, $n_{bacteria}$ = 26728, n_{tracks} > 800, $n_{chambers}$ = 2). The value characterizing the early phase of confinement is highlighted. E. Representative single-cell quantifications of growth and division rates over time (Methods), showing a similar uncoupling between growth and division independently of bacterial location within the chamber. F. Quantification of single-cell growth rate and division time as a function of both bacterial location within the chamber ("Edges" in red, "Center" in blue, Methods) and the corresponding phase of confinement. 2-way ANOVA with Benjamini - Hochberg FDR correction for multiple comparisons for each phase of confinement and corresponding P values are shown. G. Corresponding plots of single-cell area, length and width. H. Timelapse confocal images of proliferating bacteria labeled at the inner membrane (grey) in the bacterial confiner, showing spontaneous confinement release when part of the aggregate suddenly exits the chamber. Insets highlight bacterial size recovery (white arrowheads). I. Quantification of bacterial area (magenta, $n_{bacteria}$ = 4873, $n_{chamber}$ = 1) and GIP (orange, $n_{chamber}$ = 1) upon confinement release (black dotted line). The light blue region depicts typical bacterial area in the absence of confinement. Time is indicated as hh:mm. Scale bars: 5 µm. Scale bar inset: 1 µm. Mean values ± s.t.d. are represented unless otherwise stated.

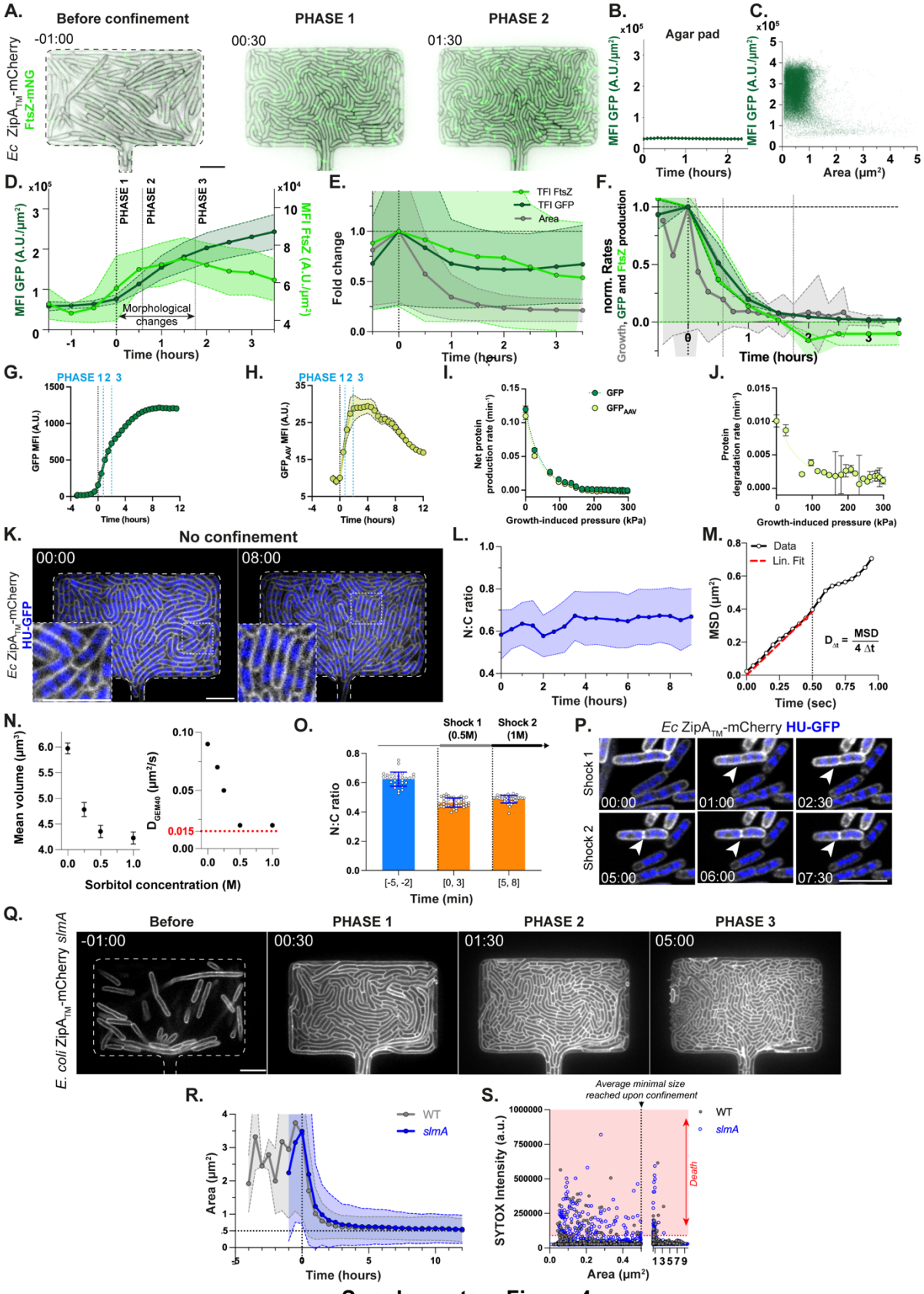

Supplementary Figure 4

Supplementary Figure 4:

A. Timelapse confocal images of proliferating bacteria labelled at the inner membrane (grey) expressing the fusion protein FtsZ-mNG (green) upon confinement (Supp. Video 4). B. GFP mean fluorescent intensity (MFI) over time upon proliferation in agar pad ($n_{bacteria}$ = 1458, N = 1). C. GFP MFI as a function of bacterial area upon confinement ($n_{bacteria}$ = 12828, $n_{chamber}$ = 1). Each point corresponds to one bacterium at a specific time point. D. Temporal evolution of single-cell GFP (dark green, $n_{bacteria}$ = 50661, $n_{chambers}$ = 4, N = 1) and FtsZ-mNG (light green, $n_{bacteria}$ = 11855, $n_{chambers}$ = 2, N = 1) MFIs respect to GIP build-up. E. Fold change in bacterial area, GFP total fluorescent intensity (TFI) ($n_{bacteria}$ = 50661, $n_{chambers}$ = 4, N = 1) and FtsZ TFI ($n_{bacteria}$ = 11497, $n_{chambers}$ = 2, N = 1) upon confinement. Raw data were normalized by their value at the time of GIP build-up. Bacterial area and FtsZ intensity were measured on different experiments. F. GFP ($n_{chambers}$ = 4, N = 1) and FtsZ ($n_{chambers}$ = 2, N = 1) production rates normalized by their value at the time of GIP build-up. Bacterial growth rate (grey) was computed on another dataset (Figure 2.D). G. GFP MFI of the chamber total area upon confinement ($n_{chambers}$ = 4, N = 2). H. GFP_{AAV} MFI of the chamber total area upon confinement ($n_{chambers}$ = 4, N = 2). To note, MFI rose rapidly in Phases 1-2, plateaued during Phase 3, and then declined. This indicates that protein production slows sharply by Phase 2 and that degradation exceeds synthesis in Phase 3. I. Mean estimated values of protein production rate based on GFP (dark green) and GFP_{AAV} (light green) MFI (Supp. Note 1). Dotted lines indicate exponential fits that closely match the one shown in Figure 1.C ($\tau \sim 40$ min). J. Mean estimated values of GFP_{AAV} degradation rate based on GFP and GFP_{AAV} MFI. To note, we found that GFP_{AAV} degradation in the absence of confinement (GIP = 0 kPa) closely matches known values in *E. coli*, i.e. 0.012 min^{-1} (1). Protein degradation rate also decreased with increased pressure, as highlighted by the exponential fit ($\tau \sim 50$ min) (Supp. Note 1). K. Timelapse confocal images of proliferating bacteria labeled at the inner membrane (grey) and DNA (blue) during in the bacterial confiner in the absence of confinement. Insets highlight DNA occupancy. L. Karyoplasmic ratio in the absence of confinement ($n_{bacteria}$ = 6025, $n_{chambers}$ = 1). M. Quantification of 40NM-GEMS diffusion coefficient from MSD analysis (Methods). N. Mean bacterial volume (*left*) and 40NM-GEMS effective diffusion coefficient (*right*) for a range of sorbitol concentrations ($n_{bacteria}$ > 130, N > 3 per condition). The diffusion value of 0.015 $\mu m^2/s$ (red) corresponds to the higher level of crowding reached upon confinement. O. Timelapse confocal images of bacteria labelled at the inner membrane (grey) and DNA (blue) upon two successive hyperosmotic shocks in CellASIC chambers. Images shown in Figure 3.J. with the DNA signal added. White arrowheads indicate the division site. Time is indicated as mm:ss. P. Corresponding karyoplasmic ($n_{bacteria} \geq 199$, N = 4 per condition). Q. Timelapse confocal images of proliferating *slmA* mutant labeled at the inner membrane (grey) upon confinement. R. Bacterial area upon confinement for the WT strain (grey, $n_{bacteria}$ > 47000, $n_{chambers}$ = 4, N = 2) and *slmA* mutant (blue, $n_{bacteria}$ = 24960, $n_{chambers}$ = 2, N = 1). S. SYTOX Green intensity versus bacterial area. Each point corresponds to one bacterium at a given time. Vertical dotted line: average minimal

size reached upon confinement. Red region: SYTOX Green intensities reached upon bacterial death. Mean values ± s.t.d. are represented. Scale bars: 5 μm; time is indicated as hh:mm, unless otherwise stated.

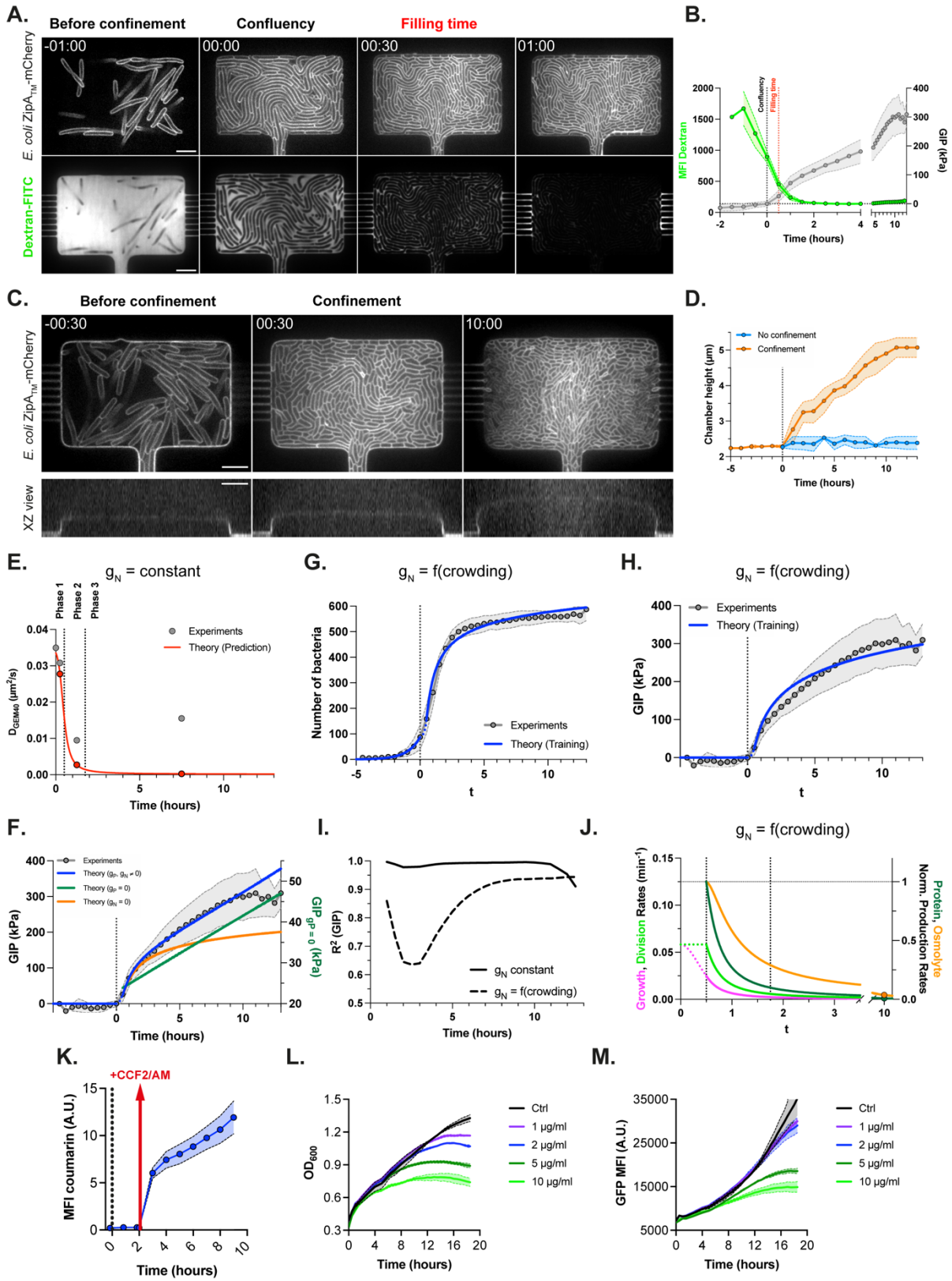

Supplementary Figure 5

Supplementary Figure 5:

A. Timelapse confocal images of proliferating bacteria labelled at the inner membrane (grey) in the bacterial confiner in the presence of a culture medium supplemented with Dextran-FITC (*bottom*). We define "Confluency" as the time at which bacteria become in close contact with their neighbors and start to build-up pressure, and "Filling time" when bacteria fully occupy the 2D chamber floor (*i.e.* the theoretical definition of confluency), indicated by a 75% decrease in the medium fluorescence compared to free space. Filling time occurs 30 minutes after confluency. B. Corresponding chamber mean fluorescent intensity (MFI) of Dextran (green, $n_{chamber} = 3$, N = 1) and GIP (grey, $n_{chamber} = 13$, N = 3). C. Timelapse confocal images of proliferating bacteria during confined growth and corresponding XZ views of the chamber walls stained with FM1-43 (*bottom*). D. Chamber height in the absence (blue) and presence (orange) of confinement ($n_{chamber} = 3$, N = 1). E. Theoretical prediction (red) and corresponding experimental data points (grey) of 40nm-GEMs effective diffusion coefficients upon confinement (Supp. Note 2, Eq.21). F. Experimental curve of GIP (grey) and theoretical fits corresponding to models where $\boldsymbol{g_P, g_N \neq 0}$ (blue), $\boldsymbol{g_P = 0}$ (green) and $\boldsymbol{g_N = 0}$ (orange). G. Experimental curve (grey) and theoretical fit (blue) of the number of bacteria in 2D, based on an alternative model where osmolyte synthesis ($\boldsymbol{g_N}$) has the same dependance to crowding than protein synthesis, and decreases exponentially with the protein concentration. H. Experimental curve (grey) and theoretical fit (blue) of GIP in the alternative model. I. Comparison of fit accuracy in the case of GIP for the two models based on R^2 (solid line: main model; dashed line: alternative model). J. Theoretical predictions of bacterial growth rate (magenta), division rate (light green), protein normalized production rate (dark green), and osmolyte normalized production rate (orange) in the alternative model. Note that in this case, protein production rate decreases faster than the small osmolytes production rate upon confined growth, still supporting the *overpressurization* of bacterial growth for long periods under protein production arrest. K. Temporal evolution of the coumarin MFI over the entire chamber for bacteria expressing cutinase and β-lactamase (blue) upon perfusion of CCF2/AM (red line) at the start of Phase 3 ($n_{chambers} = 6$, N = 2). L. Optical density (OD_{600}) over time for *E. coli* MG1655 strain constitutively expressing GFP, across increasing spectinomycin concentrations. M. Mean fluorescence intensitites (MFI) over time for *E. coli* MG1655 strain constitutively expressing GFP, across increasing spectinomycin concentrations. Mean values $\pm$ s.t.d. are represented. Time is indicated as hh:mm. All scale bars: 5 µm.

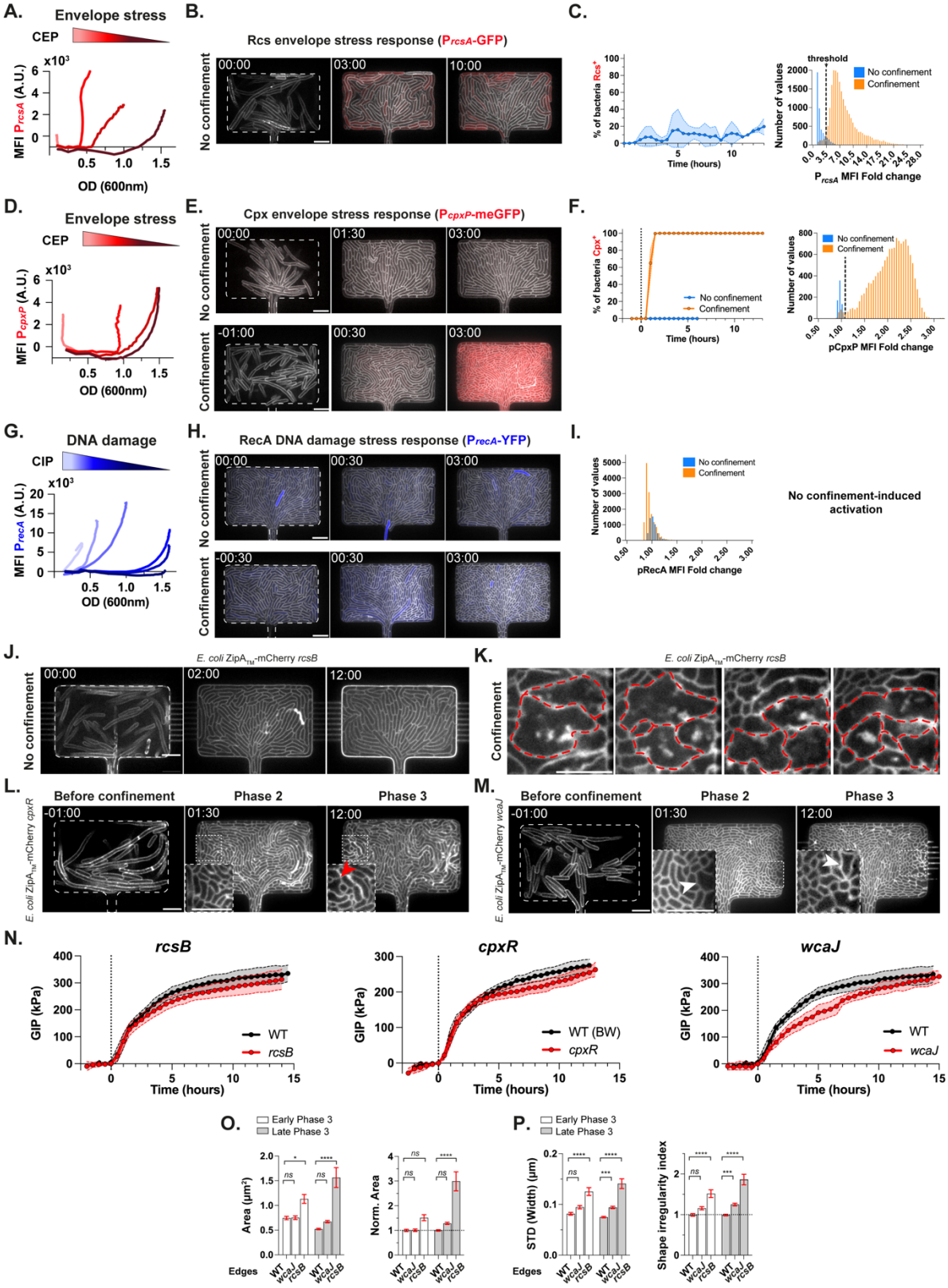

Supplementary Figure 6

Supplementary Figure 6:

A. Validation of the P_{rcsA}-GFP transcriptional reporter using cephalexin (CEP). Mean fluorescent intensity (MFI) as a function of the optical density across increasing CEP concentrations (Methods). B. Timelapse confocal images of proliferating bacteria labeled at the inner membrane (grey) expressing the P_{rcsA} transcriptional reporter (red) in the bacterial confiner in the absence of confinement. C. Percentage of bacteria activating the Rcs stress response in the absence of confinement ($n_{total\ bacteria}$ = 35200, $n_{chambers}$ = 3, N = 1) (*left*). Histograms of the P_{rcsA} reporter MFI fold change for non-confined (blue) and confined (orange) bacteria (*right*). D. Validation of the P_{cpxP}-meGFP transcriptional reporter. E. Timelapse confocal images of proliferating bacteria labeled at the inner membrane (grey) expressing the P_{cpxP}-meGFP transcriptional reporter (red) in the absence (*top*) and presence (*bottom*) of confinement (Supp. Video 5). Time 0 indicate the time of GIP build-up. F. Percentage of bacteria activating the Cpx stress response in the absence (blue, $n_{total\ bacteria}$ = 160, $n_{chamber}$ = 1) and presence of confinement (orange, $n_{total\ bacteria}$ = 41160, $n_{chambers}$ = 3, N = 1) (*left*). Histograms of the P_{cpxP} reporter MFI fold change for non-confined (blue) and confined (orange) bacteria (*right*) G. Validation of the P_{recA}-YFP transcriptional reporter using ciprofloxacin (CIP). H. Timelapse confocal images of proliferating bacteria labeled at the inner membrane (grey) expressing the P_{recA} transcriptional reporter (blue) in the absence (*top*) and presence (*bottom*) of confinement (Supp. Video 5). I. Histograms of P_{recA} reporter MFI fold change for non-confined (blue) and confined (orange) bacteria. J. Timelapse confocal images of proliferating *rcsB* mutant labeled at the inner membrane (grey) in the bacterial confiner in the absence of confinement. K. Zoomed confocal images of representative morphological phenotypes in Rcs-deficient bacteria upon confinement. These bacteria show blebbing morphologies (red), often containing cytoplasmic membrane pools. L. Timelapse confocal images of proliferating *cpxR* mutant labeled at the inner membrane (grey) upon confinement (Supp. Video 6). Insets highlight *cpxR* bacteria minor shape defects (red arrowheads). M. Timelapse confocal images of proliferating *wcaJ* non-capsulated mutant labeled at the inner membrane (grey) upon confinement (Supp. Video 6). Insets highlight *wcaJ* bacteria shape defects (white arrowheads). N. GIP for all the mutants used in this study (red), including *rcsB* ($n_{chambers}$ = 25), *cpxR* ($n_{chambers}$ = 22) and *wcaJ* ($n_{chambers}$ = 5), and comparison to the corresponding WT strain (black) ($n_{chambers} \geq 13$). In all cases: N = 1. O. Raw (*left*) and normalized (*right*) bacterial area for WT, *wcaJ* and *rcsB* strains at the edges of the chamber at early (white) and late (grey) Phase 3 (*i.e.* 2h and 10 h after GIP build-up, respectively). P. Standard deviation of bacterial width (*left*) and corresponding shape irregularity index (*right*) for WT, *wcaJ* and *rcsB* strains. Means ± standard errors are represented. These parameters were measured for the WT strain ($n_{bacteria\ –\ Early}$ = 158, $n_{bacteria\ –\ Late}$ = 478, $n_{chambers}$ = 3, N = 1), *wcaJ* ($n_{bacteria\ –\ Early}$ = 164, $n_{bacteria\ –\ Late}$ = 409, $n_{chambers}$ = 3, N = 2) and *rcsB* mutants ($n_{bacteria\ –\ Early}$ = 69, $n_{bacteria\ –\ Late}$ = 134, $n_{chambers}$ = 2, N = 1). Statistical significance was assessed using one-way ANOVA tests.

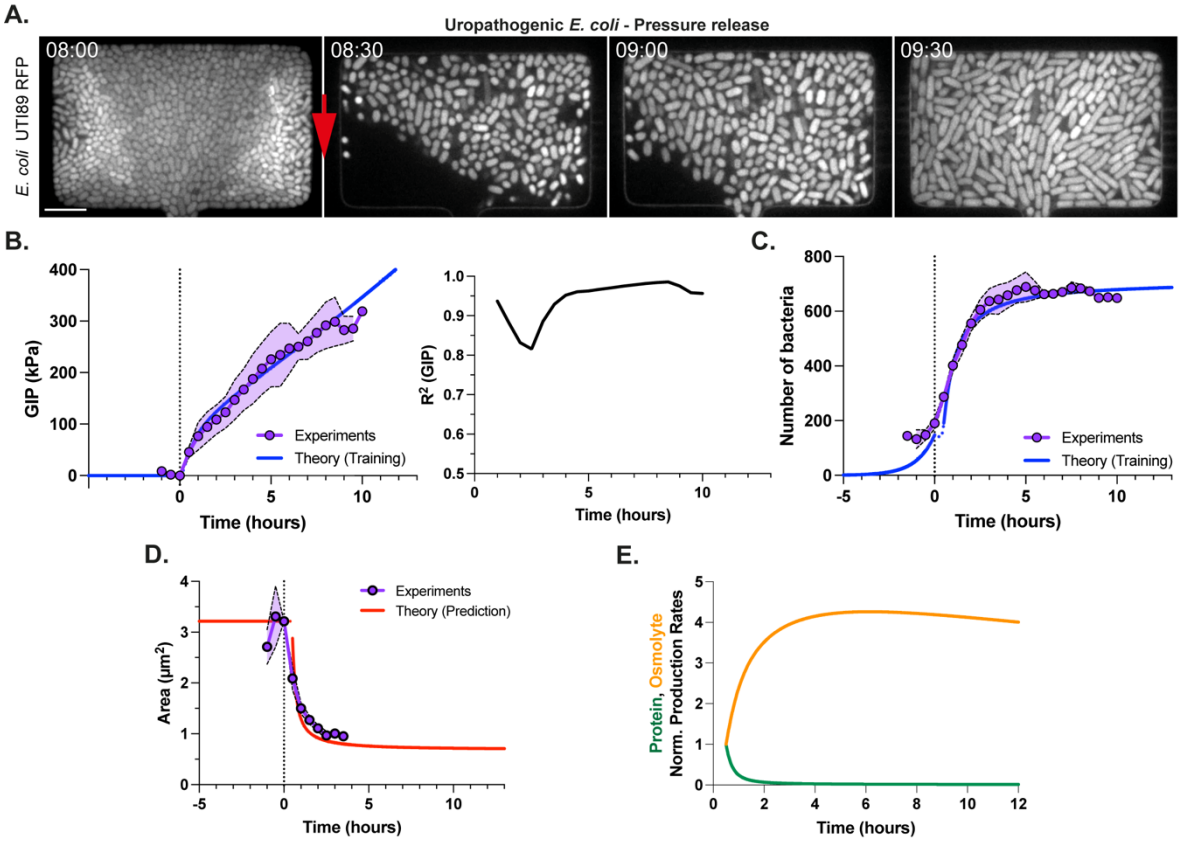

Supplementary Figure 7

Supplementary Figure 7:

A. Timelapse confocal images of the *E. coli* UTI89 RFP strain proliferating in the bacterial confiner upon confinement release (red arrow, Supp. Video 7). Time is indicated as hh:mm. B. Experimental data for the UTI89 strain (purple) and theoretical fit (blue) of GIP used to set adjustable parameters (*left*). Comparison of fit accuracy in the case of GIP for the two models based on R^2 (solid line: main model; dashed line: alternative model, *right*). C. Experimental data for the UTI89 strain (purple) and theoretical fit (blue) of the 2D number of bacteria. D. Theoretical prediction (red) and experimental curve (purple) of bacterial area over time under confinement for the UTI89 strain. E. Corresponding theoretical prediction of protein (dark green) and osmolyte normalized production rate (orange) over time.

Supplementary Note 1

Assessment of protein production using an unstable GFP variant

To refine measurements of protein production rate and test whether growth-induced pressure (GIP) continues to build during Phase 3 independently of ongoing protein synthesis, we generated a bacterial strain constitutively expressing a cytoplasmic reporter fused to an unstable GFP variant (GFP_{AAV}). This reporter is expressed under the same promoter (P_R) used in the strain employed throughout this work, which contains a classical GFP variant with a half-life of ≥ 2 hours (Figure 3.A-C, Supp. Figure 4.B-F). Details of the cloning procedure are provided in the Methods.

GFP_{AAV} was selected based on previous studies showing that the addition of short C-terminal peptide tags renders GFP susceptible to degradation by housekeeping proteases, allowing dynamic monitoring of gene expression (1). Consistent with this property, the strain expressing GFP_{AAV} displayed substantially lower fluorescence than the strain expressing stable GFP during exponential growth, indicating rapid degradation of the reporter and a reduced steady-state protein pool.

We performed confinement experiments to monitor GFP_{AAV} fluorescence dynamics across the different confinement phases and compared these measurements with those obtained using the stable GFP reporter. Fluorescence intensity was quantified across the entire growth chamber after background subtraction and expressed as mean fluorescence intensity (MFI) over time, with t = 0 corresponding to the normalized onset of GIP buildup (Supp. Figure 4.G-H). The image analysis procedure is described in the Methods.

The unstable reporter revealed a rapid increase in fluorescence during the initial stages of confinement (Phases 1 and 2), followed by a plateau during Phase 3 (approximately 2-4 hours post-confinement) and a subsequent gradual decrease. This behaviour indicates that net protein production decreases during Phase 2 and that, by Phase 3, degradation exceeds synthesis. This transition coincides with the buildup of GIP, ultimately leading to growth arrest. These observations therefore support the conclusions obtained using the stable GFP reporter.

The combined datasets allow estimation of production and degradation rates. Based on the temporal evolution of MFI as a function of growth-induced pressure, we estimated the effective protein production rate ($k_{production}$) using:

$$\frac{dMFI(t)}{dt} = \left[k_{production} - \left(k_{degradation} + k_{growth}\right)\right]MFI(t)$$

With MFI indicating the total mean fluorescence intensity at the chamber scale, and k_{growth} as growth rate, $k_{degradation}$ as degradation rate. Since we measured k_{growth},

this allows us to estimate the net production rate $k_{production} - k_{degradation}$ (Supp. Figure 4.I). We want to emphasize that our choice of a stable GFP allows us to neglect $k_{degradation}$, thus providing a measurement of $k_{production}$ alone. However, with the novel measurement of the net production rate of GFP_{AAV}, and assuming that $k_{production}$ is similar, we can now extract the degradation rate of this unstable GFP as a function of pressure (Supp. Figure 4.J).

Both production and degradation rates decrease with increasing pressure and appear to follow an approximately exponential dependence. In the absence of pressure, the measured degradation rate of GFP_{AAV} is consistent with values found in the literature (≈ 0.012 min^{-1}), corresponding to a half-life of ~ 60 minutes for GFP_{AAV} in *E. coli* (1).

Finally, while variations in the balance between cell division and protein synthesis could in principle influence predicted protein accumulation, our model couples these processes through growth-dependent synthesis and dilution terms. The new dataset supports this framework: GFP_{AAV} accumulates similarly to stable GFP during the first ~ 2 hours of confinement while division progressively slows, after which protein levels plateau and eventually decline as degradation becomes dominant.

Together, these results reinforce our conclusion that protein production strongly decreases as growth-induced pressure builds during confinement. Future versions of the model could explicitly incorporate potential modulation of protein synthesis relative to division rate - particularly under changing metabolic or mechanical conditions - to further improve predictive accuracy.

Supplementary Note 2

I. MODEL

In the following, we derive a model to understand quantitatively the growth of a bacterial colony under confinement.

A. Bacterial geometry and chamber confluency constraint

During confinement, bacteria adopt a simple geometry (see Fig. 1B). To gain analytical insight into the processes underlying bacterial growth under confinement, we approximate each bacteria as a cylindrical rod (see Fig. 4B), consisting of a protoplasmic core of width w and volume V^b surrounded by a shell of thickness δ, which primarily corresponds to the cell wall during most of the confinement (see Section II C). To assess the validity of our geometrical approximation at the level of the model (i.e., average behavior), we compared in Supp. Fig. 8 the projected area of the bacteria at the bottom of the chamber, as measured from segmentation, with the projected area obtained from our cylindrical approximation (experimental width × experimental main rod axis). Both curves matched within one pixel, strongly suggesting that a more detailed geometrical description of bacterial shapes would not improve the model's accuracy given our measurement resolution.

Moreover, in our model we work with average quantities at the colony scale. We relate bacterial-scale quantities (superscript ^{b}) to colony-scale quantities (no superscript) by assuming that bacteria are confluent. Under this assumption the chamber volume V is related to V^b and the number of bacteria in the chamber n according to the relation:

$$\alpha \cdot V = n \cdot \frac{\pi}{4} \cdot (w + 2\delta)^2 \left(\frac{V^b}{\frac{\pi}{4} \cdot w^2} + 2\delta \right) \tag{1}$$

Note that even under full confluency, the chamber is not completely filled because of the packing limit of parallel cylinders. We call α, the maximal volume fraction that bacteria can occupy. For simplicity, we assume a square-lattice arrangement of bacteria, so that $\alpha = \pi/4 \approx 0.8$. Although alternative packings (e.g., hexagonal or random) yield different values of α (approximately 0.90 and 0.82–0.85 (empirical values)), these variations only change α by a few percent and therefore do not affect the main conclusions of the model at this level of description. We also emphasize that the time t^*, corresponding to full bacterial confluency, does not coincide with the onset of pressure increase in the chamber. Experimentally we find that confluency is reached approximately 30 minutes after the GIP begins to rise in the chamber (see II D for a discussion).

We finally relate quantities in the chamber to the quantities at the bottom of the chamber (where images are taken) by assuming that the density of bacteria ρ is constant throughout the chamber and equal to the maximum packing limit:

$$\rho = \frac{n}{V} = \frac{n^{2D}}{A_c \cdot w \cdot (1 + 2\overline{\delta})} \tag{2}$$

where, n^{2D} denotes the number of bacteria within the observation plane at the bottom of the chamber, A_c its area and $\overline{\delta} = \frac{\delta}{w}$.

B. Evolution of the GIP in the chamber

In recent years, evidence has pointed to the key role of osmosis on cellular and organelle growth (2, 3, 4, 5). We take into account this physical principle in our model by imposing that the chemical potential of water is balanced

throughout the bacterial membrane. This is equivalent to enforcing the equality between the difference in osmotic pressure with the difference in total mechanical pressure applied throughout the bacterial membrane (2). Here, at the difference of single-cell growth, the total mechanical pressure is composed not only of the hydrostatic pressure P but also of the external mechanical stresses σ^{el} due to the bacterial crowding in the chamber.

$$\Pi^b - \Pi_0 = \Delta P + \sigma^{el} \tag{3}$$

Where Π accounts for the osmotic pressure within bacteria, upper script ^{b}, or in the external medium, subscript $_0$; ΔP is the difference of hydrostatic pressure throughout the bacterial membrane. For simplicity, we assume that the constituents of the cell wall are incorporated during bacterial growth to maintain ΔP (6). Moreover, as most of the osmolytes within bacteria are accounted for by small osmolytes (7), we consider that the osmotic pressure is dominated by the ideal gas term:

$$\Pi^b = k_B T \cdot \frac{N^b}{V^b - R^b} \tag{4}$$

where, N^b is the number of osmolytes per bacteria, V^b is the volume of the bacterial protoplasm, and R^b represents the excluded volume arising from the macromolecular content of the cell. Since proteins constitute the majority of the bacterial dry mass, we assume that this excluded volume is proportional to the number of proteins P^b times the average effective volume occupied by a single protein, such that $R^b \sim v_p P^b$.

During growth, mechanical stress builds up in the chamber due to cell proliferation and confinement within the chamber. We call this stress growth-induced pressure (GIP) and we relate it to the volume of the chamber V through a scalar Hooke's law:

$$\sigma^{el} = E \cdot \left(\frac{V}{V_c} - 1 \right) \tag{5}$$

Where, E is the elastic modulus of the chamber and V_c is the non-deformed volume of the chamber. Together, Eqs. 4, 1, and 5 form a complete system of equations that predicts how the chamber volume and thus the GIP depends on the number of small osmolytes N and the number of proteins P in the chamber.

C. Analytical expression of the chamber volume as a function of proteins and small osmolytes

To simplify the following analytical expressions, we normalize all variables by their values at the time of bacterial confluency (Eq.1) and introduce the following auxiliary quantities. For clarity, all variables and their definitions are summarized in Supp. Table 5.

$$\overline{V} = \frac{V}{V^*}\,,\ \overline{P} = \frac{P}{P^*}\,,\ \overline{N} = \frac{N}{N^*}\,,\ \overline{V}_c = \frac{V_c}{V^*}\,,\ \overline{\Pi}_0 = \frac{\Delta P + \Pi_0}{E} \tag{6}$$

Where, $\overline{V}, \overline{P}, \overline{N}, \overline{V}_c, \overline{\Pi}_0$ respectively denote the normalized chamber volume, proteins, small osmolytes and total pressure in the chamber. Moreover, we define the following auxiliary dimensionless variables :

$$\overline{V}^e = (1 + 2\overline{\delta})^2 \cdot \left(2\overline{\delta} \cdot \overline{V}_w + \frac{\overline{R}^*}{\alpha} \right)\,,\ \alpha = \pi/4\,,\ \overline{R}^* = \frac{v_p \cdot P^*}{V^*}\,,\ \overline{V}_w = \frac{n^* \cdot w^3}{V^*}\,,\ \overline{\delta} = \frac{\delta}{w} \tag{7}$$

Where, $\overline{V}^e$ is an excluded volume that accounts for both the bacterial dry content and the excluded volume associated with cell wall at the edges of the bacteria (Sec. I D). We first express V^b and R^b using Eq.1, the relation $\overline{R} = \overline{R}^* \cdot \overline{P}$ together with the definitions of the dimensionless parameters Eq.6, Eq.7, as follows:

$$V^b - R^b = \frac{\alpha}{(1 + 2\overline{\delta})^2} \cdot \frac{V^*}{n} \cdot \left(\overline{V} - \overline{V}^e \cdot \overline{P} \right) \tag{8}$$

Note that we assumed that $\overline{P} = \overline{n}$ (see Sec.I G for a justification). We next inject Eq.8 in Eq.3 and Eq.4. We find:

$$\overline{V}_c \cdot (1+2\overline{\delta})^2 \cdot \frac{kTN^*}{\alpha E V^*} \cdot \overline{N} = \left((\overline{\Pi}_0 - 1) \cdot \overline{V}_c + \overline{V}\right) \cdot \left(\overline{V} - \overline{V}^e \cdot \overline{P}\right) \tag{9}$$

Taking the previous equation at bacterial confluency ($t = t^*$) yields an expression for $\overline{V}_c \cdot \frac{kTN^*}{\alpha E V^*}$:

$$\overline{V}_c \cdot (1+2\overline{\delta})^2 \cdot \frac{kTN^*}{\alpha E V^*} = \left((\overline{\Pi}_0 - 1) \cdot \overline{V}_c + 1\right) \cdot \left(1 - \overline{V}^e\right) \tag{10}$$

Substituting the expression for $\overline{V}_c \cdot \frac{kTN^*}{\alpha E V^*}$ into Eq.9 finally leads to a second order polynomial in $\overline{V}$. The positive solution reads:

$$\overline{V} = -\frac{1}{2} \cdot \left((\overline{\Pi}_0 - 1) \cdot \overline{V}_c - \overline{V}^e \cdot \overline{P}\right) + \frac{1}{2} \cdot \sqrt{\left((\overline{\Pi}_0 - 1) \cdot \overline{V}_c + \overline{V}^e \cdot \overline{P}\right)^2 + 4 \cdot \left((\overline{\Pi}_0 - 1) \cdot \overline{V}_c + 1\right) \cdot \left(1 - \overline{V}^e\right) \cdot \overline{N}} \tag{11}$$

We model in the next subsections the production of proteins P and osmolytes N to describe how $\overline{V}$ and thus the mechanical stress in the chamber, also called growth-induced pressure (GIP) varies with time (Eq.5).

D. Interpretation of the auxiliary parameter $\overline{V}^e$

In this subsection, we clarify the physical meaning of the auxiliary (dimensionless) parameter $\overline{V}^e = \frac{V^e}{V^*}$ that appears in Eq.11. This parameter represents an excluded-volume contribution with two components (Eq.7): one arising from the bacterial dry mass evaluated at confluency, and one associated with the cell wall at confluency ($t = t^*$). Using Eq. 8 at confluency, the total space occupied by bacteria in the chamber can be partitioned into a volume proportional to the intracellular water content and an excluded-volume term:

$$\alpha V^* \;=\; n^* \big(V^{b,*} - R^{b,*}\big)(1+2\overline{\delta})^2 \;+\; \alpha V^e, \tag{12}$$

This expression can be recast as:

$$\alpha V^* \;=\; n^* \left(V^b + \mathcal{V}^{\text{wall}}\right), \qquad \text{where} \quad \mathcal{V}^{\text{wall}} \;=\; \alpha w^3 \left[(1+2\overline{\delta})^2 \left(\frac{V^b}{\alpha\, w^3} + 2\overline{\delta}\right) - \frac{V^b}{\alpha\, w^3}\right]. \tag{13}$$

Thus, the excluded volume associated with the cell wall contributes in two ways: one part is captured explicitly by V^e (excluded volume of the cell wall localised at the bacterial edges), while the other scales with V^b and appears through the geometric prefactor $(1+2\overline{\delta})^2$ in Eq.12.

E. Proteins production rate

Proteins have been proposed to play a minor role in the osmotic pressure due to their small concentrations in cells relative to small osmolytes (e.g. metabolites) (2). They nevertheless play an important role in cellular growth by producing/importing those small osmolytes. We thus describe the total protein production rate within the chamber with the following equation:

$$\frac{\mathrm{d}\overline{P}}{\mathrm{dt}} = k_p \cdot \overline{P} \tag{14}$$

Where k_p accounts for the protein growth rate. In the regime where k_p is constant, Eq.14 describes an exponential increase of the proteins, which molecularly arise from the fact that ribosomes autocatalyze their formation. In agreement with previous studies in yeast (8), we observe that protein production is sensitive to macromolecular crowding. To include this feature in our growth model and supported by this recent literature, we consider that the

protein production rate is diffusion-limited and use a Doolittle-like equation (8) to relate the variations of the protein production rates with the protein concentration, and thus the macromolecular crowding:

$$k_p = k_p^* \cdot e^{-\xi_p \cdot v_p \cdot (p^b - p^{b,*})} \tag{15}$$

Where k_p^* is the protein growth rate in the absence of confinement, v_p the average volume of one crowder, p^b and $p^{b,*}$ the protein concentrations respectively during growth and at the onset of bacterial confluency, and ξ_p an adimensional coefficient that describes the sensitivity of protein production to crowding.

We now express k_p in terms of the variables of our model. Using Eq.8 and the fact that the total protein number in the chamber is $P = P^b \cdot n$, we express the protein concentration per bacteria $p^b = \frac{P^b}{V^b - R^b}$ normalized by the protein concentration at the onset of confluence as:

$$\frac{p^b}{p^{b,*}} = \frac{P^b}{P^{b,*}} \cdot \frac{n}{n^*} \cdot \frac{1 - \overline{V}^e}{\overline{V} - \overline{V}^e \cdot \overline{P}} = \overline{P} \cdot \frac{1 - \overline{V}^e}{\overline{V} - \overline{V}^e \cdot \overline{P}} \tag{16}$$

F. Small osmolytes production rate

In our model, we take into account the production or import of small osmolytes by proteins through the following equation:

$$\frac{\mathrm{d}\overline{\mathrm{N}}}{\mathrm{d}t} = \overline{k}_{osm} \cdot k_p^* \cdot \overline{P} \qquad \text{With,} \quad \overline{k}_{osm} = \frac{k_{osm}}{k_p^*} \cdot \frac{P^*}{N^*} \tag{17}$$

With k_{osm} as the small osmolyte growth rate. We considered two scenarios for the dependency of k_{osm} during growth. (1) k_{osm} is constant throughout the experiment. (2) Or it decreases exponentially with crowding, identically to the protein growth rate dependency: $k_{osm} = k_{osm}^* \cdot e^{-\xi_p \cdot v_p \cdot (p^b - p^{b,*})}$. Unless specified, in the following we will refer to scenario (1) as it better fits our data (see Supplementary Figure 5.F-I in the main article).

Note that if proteins grow exponentially, the latter equation predicts that the number of those small osmolytes ruling cell volume, also grows exponentially at the same rate which was recently proposed to explain the origin of protein concentration homeostasis in free unicellular growth (2). On the other hand, in the regime of protein production arrest due to crowding, Eq.17 predicts that the number of small osmolytes keeps increasing in the chamber. As the chamber prevents volume growth, this increase in number is further accompanied by an increase in osmotic pressure (Eq.4) which also increases the mechanical stress in the chamber to sustain the pressure balance (Eq.3). This natural decoupling between volume growth and osmolyte production is what we propose to be at the core of the singular regime of growth that we observe with protein production arrest and chamber pressure increase.

G. Bacterial number

Important mechanistic details have been understood in recent years on the main drivers leading to bacterial division. In Yeasts and Eukaryotes, a body of evidence shows that the division signal is achieved by the dilution of specific division inhibitors during growth (Whi5 in Yeast, and its mammalian cell homolog, Rb (9 and 10). In bacteria, however, the prevailing mechanism is not related to protein concentration but instead to the number of proteins necessary to assemble the cytoskeletal scaffold of the Z ring that constricts to divide the cell in two (see Ftsz protein and 11). Based on this mechanism and for the sake of simplicity in our model, we propose to implement bacterial division every time the protein number has been doubled. This choice is twofold. (1) It allows for homeostasis of protein concentration during free growth based on a criterion relying on a number of proteins. (2) Most proteins were shown to scale with each other during growth. Under this assumption, the total number of proteins is a proxy of the number of enzymes ruling the number of small osmolytes. Our model would thus remain valid up to a scaling factor that would renormalize the osmolyte production rate, $\overline{k}_{osm}$. According to the previous reasoning, on average, after j divisions the total bacterial protein content has been multiplied by 2^j as well as the total number of bacteria:

$$2^j = \overline{P}(t^{d,j}) = \overline{n} \tag{18}$$

Where, $\overline{n}$ accounts for the number of bacteria normalized by the number of bacteria at confluency, and $t^{d,j}$ the time at which the j^{th} division occurs. In the continuum limit, assuming that there are many bacterial divisions at the timescale of our experiments ($\sim 13h$), the previous equation simply states that the number of bacteria is a proxy of the normalized number of proteins that have been produced:

$$\overline{n}(t) = \overline{P}(t) \tag{19}$$

H. Summary of key equations

The problem to solve reads:

$$\frac{\mathrm{d}\overline{P}}{\mathrm{d}t} = k_p(\overline{P}, \overline{N}) \cdot \overline{P} \tag{20}$$

$$\frac{\mathrm{d}\overline{N}}{\mathrm{d}t} = \overline{k}_{osm} \cdot k_p^* \cdot \overline{P} \tag{21}$$

With: $\overline{P}(0) = 1$, $\overline{N}(0) = 1$. This system of equations is solved using the Mathematica software.

The growth-induced pressure σ^{el}, and the apparent number of bacteria n^{2D} (Fig.4 panel C of the main text), are derived from the solutions of Eq.20 and Eq.21, and the relationships outlined below:

$$\sigma^{el} = E \cdot \left(\frac{\overline{V}}{\overline{V}_c} - 1 \right) \quad , \quad n^{2D} = n^{2D,*} \cdot \frac{\overline{n}}{\overline{V}} \tag{22}$$

The division rate (Fig.4 panel F of the main text) is computed using the following relationship:

$$g_d = \frac{1}{\overline{n}_b} \cdot \frac{\mathrm{d}\overline{n}_b}{\mathrm{d}t} = \frac{ln(2)}{\tau_{div}} \tag{23}$$

The experimentally determined growth rate (see Fig.4.F in the main text) was computed as:

$$g_a^{exp} = \frac{1}{< A^{b,proj}(t=0) >} \cdot < \frac{A^{b,proj}_{t_{division}} - A^{b,proj}_{t_{birth}}}{t_{division} - t_{birth}} > \tag{24}$$

Where, <> denotes the average over bacteria in the chamber. In our mean-field theory, we only have access to the mean bacterial area, which results from two opposing effects: growth and division. Consequently, we cannot only use the mean-field bacterial area to compute the average growth rate per bacteria. Nevertheless, in the regime addressed by our model, bacteria are confluent, meaning that chamber growth reflects bacterial growth. Therefore, we estimate the average volume growth rate per bacteria as the rate of change of the chamber volume divided by the total number of bacteria: $\frac{1}{n} \cdot \frac{dV}{dt}$. Further using the geometrical constraint that $V^b = \frac{\pi}{4} \cdot w \cdot A^{b,proj}$ and Eq.2 we obtain the following estimate of the predicted bacterial growth rate, which is compared with g_a^{exp} in Fig.4.E of the main text:

$$g_a^{theo} = \frac{1}{A^{b,proj}(t=0)} \cdot \frac{A_c \cdot (1 + 2\overline{\delta})}{\frac{\pi}{4} \cdot n^{2D^*}} \cdot \frac{1}{\overline{n}} \frac{d\overline{V}}{dt} \tag{25}$$

The diffusion of GEM40 particles (Supplementary Fig.5, panel E) was computed using a Doolittle-like equation (8). For simplicity and following (8), we assumed that the dependence of the GEM particle diffusion coefficients on crowding followed the same relationship as that of the protein production rates:

$$\frac{D_{GEM40}}{D^*_{GEM40}} = \frac{k_p}{k_p^*} = e^{-\xi_p \cdot v_p \cdot (p^b - p^{b,*})} \tag{26}$$

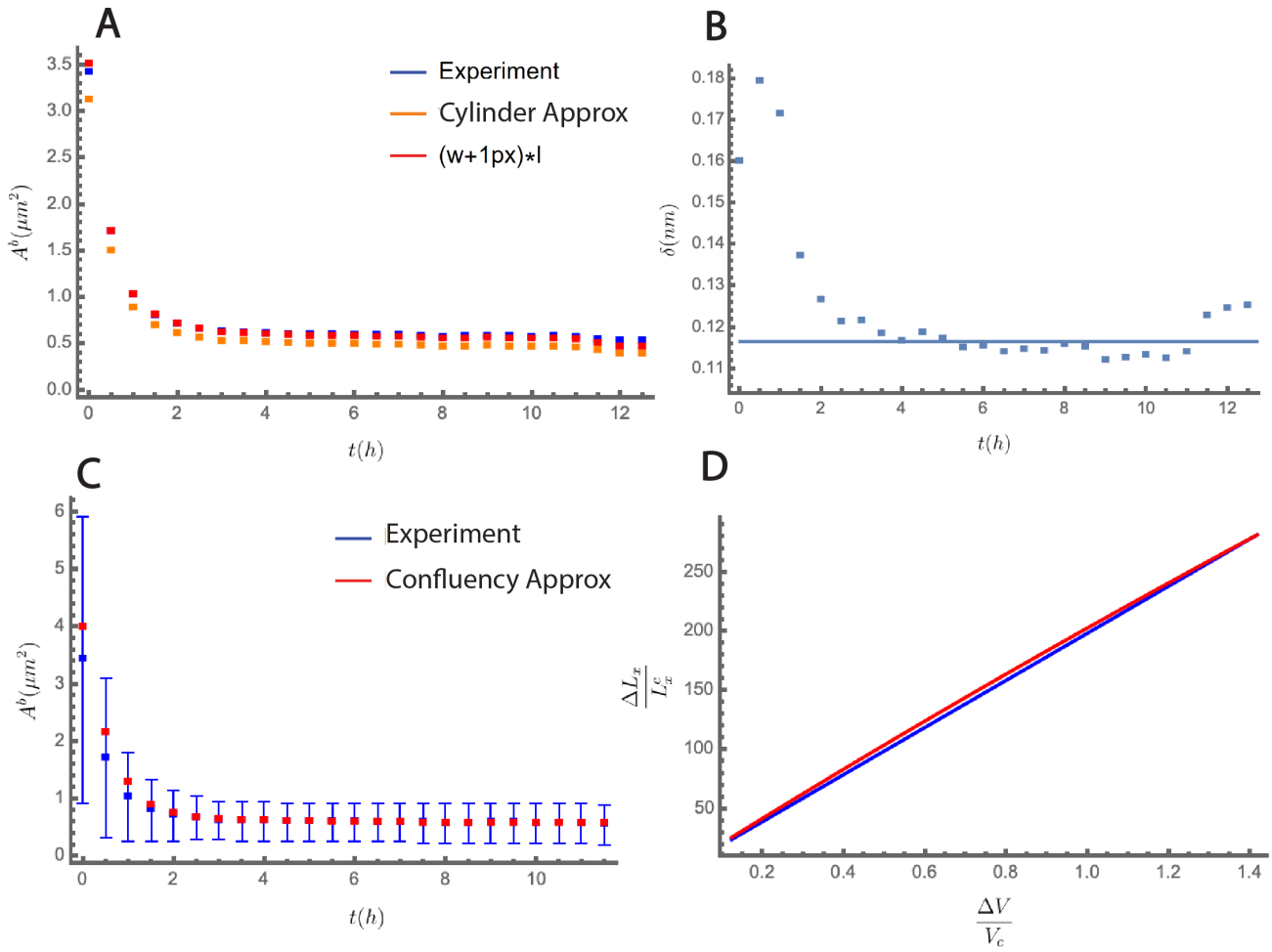

Supplementary Figure 8: **Calibration of the model** (A) Comparison between the experimental bacterial projected area (blue) and the projected area assuming that the average shape of the bacteria is a cylinder (orange). This shape approximation is within the experimental measurement error of the actual data as adding one pixel to the experimental width makes the shape approximation match the experimental data. (B) Estimation of the width of the interstitial space using Eq.34 (see Figure 4.B of the main article for a definition). (C) Comparison between the experimental bacterial projected area (blue) and the projected area assuming confluency (Eq.1). Both curves match after 30 minutes. (D) Horizontal versus volume strains under no approximations (red) and following a linear approximation (blue).

II. CALIBRATION OF THE MODEL

The model we have developed displays a significant number of parameters.

$$\{t^*, \xi_p, k_p^*, n^{2D,*}, E, \overline{R}^*, \overline{\Pi_0}, \overline{k}_{osm}, \overline{\delta}, \overline{V}_w, \overline{V}_c\} \tag{27}$$

The object of this section is to determine the value of these parameters to decrease the number of adjustable parameters.

A. Young modulus of the chamber E

We first calibrate the young modulus of the chamber by applying a known pressure and by measuring the horizontal displacement:

$$\sigma^{el} = E^{eff} \cdot \frac{\Delta L_x}{L_x^c} \tag{28}$$

We find, $E^{eff} = 4.439$MPa. Note that E^{eff} is not equal to the young modulus E defined in Eq. 5 as the horizontal strain of the chamber is not equal to the volume strain. To relate the latter strains we consider the chamber as a truncated pyramid whose upper surface expands with time and thus express the volume of the chamber as:

$$V(t) = h(t) \cdot \frac{\left(Ac + A(t) + \sqrt{Ac \cdot A(t)}\right)}{3} \tag{29}$$

In our experiment the bottom surface cannot move and the surface A_c thus remains equal to its equilibrium value. On the other hand, the upper surface and the height of the chamber expand due to the stress exerted by the bacterial colony growth:

$$A(t) = (L_x^c + \Delta L_x) \cdot (L_y^c + \Delta L_y) \quad And, \quad h(t) = h_c + \Delta h \tag{30}$$

In practice we observe that after 13 hours of growth, $\Delta L_x \sim \Delta L_y \sim \Delta h \sim 2\mu m$. For the sake of precision, we will assume that $\Delta L_y = \alpha_y \cdot \Delta L_x$ and $\Delta L_z = \alpha_z \cdot \Delta L_x$. We measure $\alpha_y \approx 0.93$ and $\alpha_z \approx 1.25$ by making the ratio of the final displacements. By expanding Eq.29 at linear order in the horizontal strain, we show that:

$$\frac{\Delta L_x}{L_x^c} \approx \frac{\frac{\Delta V}{V^c}}{\frac{1}{2} + \frac{1}{2} \cdot \alpha_y \cdot \frac{L_x^c}{L_y^c} + \alpha_z \cdot \frac{L_x^c}{L_z^c}} \tag{31}$$

In practice the previous expansion is a good approximation because we find experimentally that $\frac{\Delta L_x}{L_x^c} < 0.07$. Nevertheless, because the vertical strains in our experiments are high - the chamber height is roughly doubled (see Supplementary Figure 5.C-D in the main text) we quantify the accuracy of our approximation. We find that the effect of non-linear terms in the expansion are in the order of 8% and for completeness we effectively incorporate these non linear terms by multiplying $\frac{\Delta L_x}{L_x^c}$ with a factor α_{NL} that we calibrate to be equal to 0.92. Figure 1.D shows that our linear approximate relationship between horizontal and volume strains is in good agreement with the true relationship. Eq.31 finally allows us to relate the effective Young modulus that we measure and the one that we use in our model:

$$E = \alpha_{NL} \cdot \frac{E^{eff}}{\frac{1}{2} + \frac{1}{2} \cdot \alpha_y \cdot \frac{L_x^c}{L_y^c} + \alpha_z \cdot \frac{L_x^c}{L_z^c}} \tag{32}$$

Given the non-deformed dimensions of the chamber $L_x^c = 31.4\,\mu$m, $L_y^c = 19.2\,\mu$m, $L_z^c = 2.3\,\mu$m, we find that $E \approx 200kPa$ (see Fig.1.D).

B. Bacteria diameter w

Using our tracking algorithm, we are able to measure w at the single bacteria level. In average, we find that w is independent of time once confluency is reached (i.e. maximum of surface occupancy Fig.1.C). The median of the dataset is $w \approx 0.33\mu m$ (Fig.1.B).

C. Interstitial space between bacteria δ

In our experiments, we observe that even after confluency is reached the interstitial space between bacteria is non negligible. We thus take into account this observation in our model by considering a shell around each bacteria of width δ (see Fig.5.A of the main text). We next estimate the shell width thanks to the relation:

$$A_c = n^{2D} \cdot \left(A^{b,proj} \cdot (1 + 2\overline{\delta}) + 2\overline{\delta} \cdot w^2 \cdot (1 + 2\overline{\delta}) \right) \tag{33}$$

The latter equation is a polynomial equation in $\overline{\delta}$ which leads to:

$$\frac{\delta}{w} = -\frac{1}{4} \cdot \left(1 + \frac{A^{b,proj}}{w^2} \right) + \sqrt{\frac{A_c}{4n^{2D}w^2} + \frac{1}{16} \cdot \left(\frac{A^{b,proj}}{w^2} - 1 \right)^2} \tag{34}$$

Interestingly, using our measurements of average bacterial number n^{2D}, diameter w, and protoplasm projected area $A^{b,proj}$ we find that δ is independent of time during most of the confinement. Its median value is $\delta = 117$nm. Note that cell wall width in *E. Coli* is typically about 80nm. Given that the precision of our measurement is about the size of one pixel $\sim 60nm$, we conclude that most of the interstitial space that we measure is occupied by the cell wall.

D. Confluency t ime t^*

We initialise the model predictions at $t^* = 0.5\,\mathrm{h}$ for three reasons:

- Measurements at the start of the experiment ($t = 0$) are noisier, which limits the precision of parameter estimation and calibration (Fig.1.C). In particular we note that at $t^* = 0.5\,\mathrm{h}$ the bacterial area matches the bacterial area outside of the chamber which is more realistic.
- In our data, GIP begins to increase before bacteria are fully confluent, so Eq.1 is not strictly satisfied during the earliest phase of confinement.
- Early in the experiment, cells adopt a more complex geometry (mild filamentation and curvature) that is not captured by our geometrical approximation; to avoid geometry-induced artefacts, we begin predictions at a later time when the approximation is more accurate (Fig.1.C).

E. Summary of the input parameter values

We summarize in Supplementary Table 1 the values of the calibrated input parameters of the model.

Supplementary Table 1: Description and values of the optimal dimensional parameters of our model.

Symbol	Typical Value	Meaning
$n^{2D,*}$	159	Apparent bacteria number in the plan of observation
t^*	0.5h	Time of confluency
k_p^*	$3.5\mathrm{h}^{-1}$	Bacterial division rate at confluency
$\overline{\delta}$	0.35	$\overline{\delta} = \frac{\delta}{w}$
$\overline{V}_c$	0.89	$\overline{V}_c = \frac{V_c}{V_b}$
$\overline{V}_w$	$3.8 \cdot 10^{-3}$	$\overline{V}_w = \frac{n^{2D,*} \cdot w^2}{A_c \cdot (1+2\overline{\delta})}$
E	200kPa	Elastic modulus of the chamber as defined in Eq.5
$\overline{\Pi}_0$	4.42	$\overline{\Pi}_0 = \frac{\Pi_0}{E}$. With, $\Pi_0 = 963$kPa corresponding to a medium of 390mOsm.

III. FIT TO THE EXPERIMENTAL DATA

A. Method

We estimated the remaining three free parameters by fitting the model simultaneously to the GIP and bacterial-count datasets. Fitting was performed by nonlinear least squares using the Levenberg–Marquardt algorithm (Wolfram

Language, `NonlinearModelFit`, default settings), i.e. by minimizing the non-regularized and unpenalized residual sum of squares (RSS).

Let y_i denote the observations at inputs x_i and $f(x_i, \beta)$ the model with p parameters β. The residuals are $r_i = y_i - f(x_i, \hat{\beta})$, and the unbiased estimator of the observation-noise variance is:

$$\hat{\sigma}^2 = \frac{\mathrm{RSS}}{n-p}, \qquad \mathrm{RSS} = \sum_{i=1}^{n} r_i^2, \tag{35}$$

where n is the total number of data points and p the number of fitted parameters.

Under the standard Gauss–Newton (first-order) approximation, the asymptotic covariance of the parameter estimates is

$$\mathrm{Cov}(\hat{\beta}) \;\approx\; \hat{\sigma}^2 \big(J^\top J\big)^{-1}, \qquad J_{ij} = \left.\frac{\partial f(x_i,\beta)}{\partial \beta_j}\right|_{\beta=\hat{\beta}}. \tag{36}$$

Given that the parameter standard errors are $\mathrm{SE}(\hat{\beta}_j) = \sqrt{[\mathrm{Cov}(\hat{\beta})]_{jj}}$, the two-sided 95% confidence interval is then:

$$\hat{\beta}_j \;\pm\; t_{1-\alpha/2,\,n-p}\,\mathrm{SE}(\hat{\beta}_j), \qquad \alpha = 0.05, \tag{37}$$

where $t_{1-\alpha/2,\,n-p}$ is the Student's t critical value with $n-p$ degrees of freedom.

B. Fitting two versions of the model

1. *Discussion*

A key prediction of the model is that growth-induced pressure continues to increase for several hours, even when protein production has largely slowed down (Fig. 4C). This behaviour arises from a fundamental difference between the two classes of osmolytes considered here: proteins promote their own production, whereas small osmolytes, mostly metabolites and counterions, rely on proteins for their production, import, or degradation. Therefore, in the limiting regime of constant protein number, the model predicts a linear increase in the number of trapped osmolytes, resulting in a linear increase in osmotic pressure and thus in growth-induced pressure, as observed experimentally during the first hours of the third phase (Fig. 4G–H).

However, under the assumption that k_{osm} remains constant throughout the experiment, the model cannot account for the saturation of GIP observed after about 10 hours of growth. We therefore hypothesized that k_{osm} may vary during the experiment. To test this idea, we implemented a second version of the model in which k_{osm} decreases with crowding, analogously to the crowding dependence of the protein production rate:

$$k_{\mathrm{osm}} = k^*_{\mathrm{osm}}\, e^{-\xi_p v_p (p^b - p^{b,*})}. \tag{38}$$

To avoid introducing an additional fitting parameter and to allow a fair comparison between the two versions of the model, we assumed that the product $\xi_p v_p$ is identical in the crowding dependence of both k_{osm} and k_p.

2. *Case 1: k_{osm} is constant*

We find that optimal values of the remaining adjustable parameters are:

$$\{\xi_p \cdot v_p \cdot p^* = (7.871 \pm 0.717)\cdot 10^{-1} \quad , \quad \overline{R}^* = (3.304 \pm 0.458)\cdot 10^{-2} \quad , \quad \overline{k}_{osm} = (3.216 \pm 1.275)\cdot 10^{-3}\} \tag{39}$$

The previous adimensional parameters can be used to estimate important biological dimensional parameters such as the protein or the small osmolyte concentration. Note that to estimate the protein concentration and number we had to take a protein radius of $r_p \sim 3.5nm$ based on data in the literature (12). Changing r_p and thus v_p is not critical for the following qualitative conclusions. The values found rounded to one digit precision are summarized in Supplementary Table 2.

Supplementary Table 2: Description and values of the fitted dimensional parameters in the limit where k_{osm} is constant for *E. Coli* bacterial cell line.

Symbol	Typical Value	Meaning
p^*	$\sim$ 2mMol	protein concentration at confluency
n^*_{osm}	$\sim$ 400mMol	osmolyte concentration at confluency
$\%^{drymass}_{vol}$	$\sim$ 10%	Volume fraction of the dry mass, $\%^{drymass}_{vol} = \frac{R^{b,*}}{V^{b,*}}$
$\frac{N^{b,*}}{P^{b,*}}$	$\sim$ 300	number fraction of osmolytes over proteins
$\frac{k_{osm}}{k^*_p}$	1	Ratio of osmolyte over protein production rates

3. *Case 2: k_{osm} decreases exponentially with crowding*

In the other scenario where $k_{osm} = k^*_{osm} \cdot e^{-\xi_p \cdot v_p \cdot (p^b - p^{b,*})}$, the best adjustable parameters we find are:

$$\{\xi_p \cdot v_p \cdot p^* = (1.009 \pm 0.309) \ , \ \overline{R}^* = (2.381 \pm 1.648) \cdot 10^{-2} \ , \ \overline{k}_{osm} = (1.070 \pm 0.804) \cdot 10^{-1}\} \quad (40)$$

In dimensional unit, we find the values summarized in Supp. Table 3 (rounded to one digit precision):

Supplementary Table 3: Description and values of the fitted dimensional parameters in the limit where k_{osm} decreases exponentially with crowding for *E. Coli* bacterial cell line

Symbol	Typical Value	Meaning
p^*	$\sim$ 1mMol	protein concentration at confluency
n^*_{osm}	$\sim$ 400mMol	osmolyte concentration at confluency
$\%^{drymass}_{vol}$	$\sim$ 10%	Volume fraction of the dry mass, $\%^{drymass}_{vol} = \frac{R^{b,*}}{V^{b,*}}$
$\frac{N^{b,*}}{P^{b,*}}$	$\sim$ 400	number fraction of osmolytes over proteins
$\frac{k_{osm}}{k^*_p}$	40	Ratio of osmolyte over protein production rates

C. Model's fitting on UPEC bacterial cell line

We fit the $k_{osm} = constant$ version of the model to the UPEC bacterial cell line. We use the same elasticity for the chamber and adjust the geometrical properties of the bacteria. We find that the the best adjustable parameters are :

$$\{\xi_p \cdot v_p \cdot p^* = (9.563 \pm 2.181) \cdot 10^{-1} \quad , \quad \overline{R}^* = (5.136 \pm 3.858) \cdot 10^{-2} \quad , \quad \overline{k}_{osm} = (4.754 \pm 4.459) \cdot 10^{-3}\} \quad (41)$$

In dimensional unit, we find the following values (rounded to one digit precision):

Supplementary Table 4: Description and values of the fitted dimensional parameters in the limit where k_{osm} decreases exponentially with crowding for UPEC bacterial cell line.

Symbol	Typical Value	Meaning
p^*	$\sim$ 1mMol	protein concentration at confluency
n^*_{osm}	$\sim$ 400mMol	osmolyte concentration at confluency
$\%^{drymass}_{vol}$	$\sim 10\%$	Volume fraction of the dry mass, $\%^{drymass}_{vol} = \frac{R^{b,*}}{V^{b,*}}$
$\frac{N^{b,*}}{P^{b,*}}$	~ 600	number fraction of osmolytes over proteins
$\frac{k_{osm}}{k^*_p}$	~ 3	Ratio of osmolyte over protein production rates

IV. FURTHER DISCUSSION ON MODEL'S HYPOTHESES AND MODEL'S LIMITATIONS

A. Bacterial dry volume content

In our model, the bacterial volume is written as the sum of an osmotically active water volume and a non-osmotically active ("excluded") volume R, which we take proportional to the protein content. Here we justify neglecting the contribution of DNA in R.

We approximate the *E. coli* DNA as a cylinder of length $N_{\rm bp}\, l_{\rm bp}$, with $N_{\rm bp} \approx 5 \times 10^6$ base pairs, base-pair length $l_{\rm bp} \approx 0.34\,\text{nm}$, and DNA radius $r_{\rm DNA} \approx 1\,\text{nm}$. The corresponding physical volume occupied by the DNA is:

$$V_{\rm DNA} \approx N_{\rm bp}\, l_{\rm bp}\, \pi r_{\rm DNA}^2 \approx 5 \times 10^{-3}\,\mu\text{m}^3, \tag{42}$$

A typical *E. coli* volume is $V^b \sim 1\,\mu\text{m}^3$, so the DNA polymer occupies on the order of 0.5% of the cell volume, and only a few percent even when cells are confined. While this estimate is rough, it shows that most of the intracellular space occupied by the chromatin is made up mostly by water and DNA-bound proteins rather than the DNA polymer itself. We plot below the prediction of our model regarding the evolution of the fraction of dry volume during bacterial growth. We find an increase of about four folds of the dry volume fraction from 12% to about 50%. This self-consistently confirms that DNA is negligible in this contribution. Moreover, we checked with our segmentation measurements that the bacterial volume decreases by approximately fourfold during growth, which is coherent with the predicted dry volume fraction increase since the total protein content per bacteria remains nearly constant in this regime.

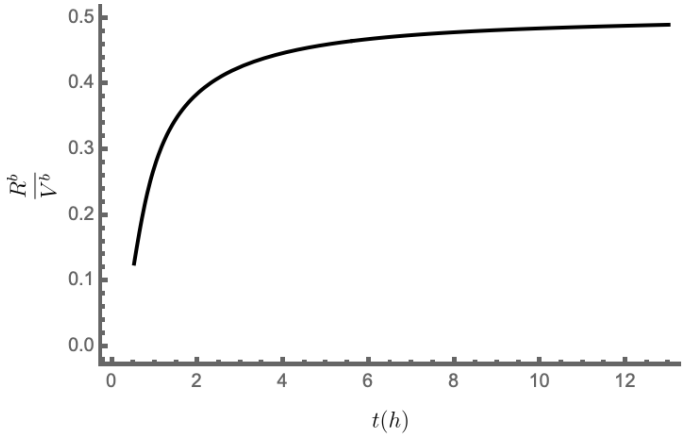

Supp. Figure 9: Dry volume fraction according to time as predicted by our model (k_{osm} constant scenario)

B. Model's limitations

While our model allows to reproduce quantitatively our data, it is worth discussing the discrepancies that we observe for the GIP. We found that the model assuming a constant $k_{\rm osm}$ provides the best fit for the first ten hours of growth (Supplementary Fig.5.I), which is why we chose this formulation. This scenario cannot capture the saturation of the GIP at long timescales that we observe because enzymes keep producing osmolytes. While we think that the decrease of k_{osm} during confinement is a plausible hypothesis the precise modelling of this dependency (crowding, enzyme degradation, regulations etc...) would however require additional data for calibration. Moreover, it is possible that other effects may take a role. For instance, we observe that around ten hours of confinement, there is a noticeable decrease in the average width of the bacterial protoplasm (Supplementary Fig. 3C). To test whether this morphological change could account for the GIP saturation, we incorporated a decrease in bacterial width into our model, under the assumption that this reduction is not accompanied by a loss of osmolytes or proteins. The simulations showed the opposite effect: the decrease in cell width increases the intracellular concentration and therefore enhances, rather than reduces, the pressure exerted by the cells on the chamber walls. This result suggests instead that the observed decrease in width may be due to leakage or partial loss of material from some bacteria, which would in turn lower the effective osmotic pressure and contribute to GIP saturation. We let these hypotheses open for further modelling and future studies.

Supplementary Table 5: Table of the variables displayed in the supplemental model.

Symbol	Definition
E, E^{eff}	**Young moduli** associated with volumetric and horizontal strains of the confining chamber (Eq.5 and Eq.28).
$\Pi^b, \Delta P, \Pi_0, \overline{\Pi}_0$	**Pressures**: Bacterial osmotic pressure, hydrostatic pressure difference at the bacterial cell wall, outer medium osmotic pressure, normalized outer medium osmotic pressure as defined in Eq.6
σ^{el}	**Mechanical stress within the confining chamber** also called growth induced pressure (GIP) in the main text.
kT	**Thermal energy**.
$n, n^{2d}, n^*, n^{2d^*}, \overline{n}$	**Average number of bacteria** in the chamber, in the plane of observation of the microscope (bottom of the chamber), in the chamber and in the observation plane at bacterial confluency ($t = t^*$). Normalized number of bacteria in the chamber $\overline{n} = \frac{n}{n^*}$.
$N^b, N, N^*, \overline{N}$	**Average number of small osmolytes** (.i.e. metabolites, ions etc) respectively per bacteria, in the chamber ($N = N^b \cdot n$), in the chamber at bacterial confluency ($t = t^*$), normalized: $\overline{N} = \frac{N}{N^*}$.
$P^b, P, P^*, \overline{P}$	**Average number of proteins** respectively per bacteria, in the chamber ($P = P^b \cdot n$), in the chamber at bacterial confluency ($t = t^*$), normalized: $\overline{P} = \frac{P}{P^*}$.
$V^b, V, V_c, V^*, \overline{V}, \overline{V}_c$	**Volume** per bacteria, of the chamber during the deformation, of the undeformed chamber, of the chamber at bacterial confluency ($t = t^*$), normalized: $\overline{V} = \frac{V}{V^*}, \overline{V}_c = \frac{V_c}{V^*}$.
v_p	**Average molecular volume** of the dry bacterial content (mostly proteins and large macromolecules).
$R^b, R, R^*, \overline{R}, \overline{R}^*$	**Dry Volume** also called non-osmotically active volume or excluded volume respectively per bacteria ($R^b = v_p \cdot P^b$), in the chamber ($R = R^b \cdot n$), in the the chamber at bacterial confluency ($t = t^*$), normalized $\overline{R} = \frac{R}{V^*}, \overline{R}^* = \frac{R^*}{V^*}$.
$w, \delta, \overline{\delta}, \alpha$	**Geometrical quantities**: bacterial protoplasmic diameter, width of the shell surrounding two bacterial protoplasms (mostly cell wall width after confluency), normalized cell wall width $\overline{\delta} = \frac{\delta}{w}$, $\alpha = \frac{\pi}{4}$ is the maximum packing limiti of parallel cylinders in a square latice configuration.
$\overline{V}_w, \overline{V}^e$	**Auxiliary normalized volumes** introduced for calculation convenience : $\overline{V}_w = \frac{n^* w^3}{V^*}$, $\overline{V}^e = (1 + 2\overline{\delta})^2 \cdot \left(2\overline{\delta} \cdot \overline{V}_w + \frac{\overline{R}^*}{\alpha}\right)$ (see Sec. I D for a discussion on the physical interpretation of $\overline{V}^e$).
$p^b, p^{b,*}$	**Protein concentration in the bacterial protoplasm** during growth, at bacterial confluency ($t = t^*$): $p^b = \frac{P^b}{V^b - R^b}$.
g_d, g_a	**Average projected area growth and division rates per bacteria** as defined in Eq.23, Eq.24, Eq.25.
ξ_p	**Strength of protein production dependency to crowding** as defined in Eq:15.
$k_p, k_{osm}, \overline{k}_{osm}$	**Protein and small osmolytes production rates** as defined in Eq.14, Eq.17.
$D_{GEM,40}, D^*_{GEM,40}$	**Diffusion constant of GEM40 particles** during growth and at bacterial confluency (see Eq.26).
ρ	**Density of bacteria in the chamber**, $\rho = \frac{n}{V}$.
$A^{b,proj}, A_c, A$	**Area** per bacteria projected in 2D (Eq.33), of the undeformed chamber, of the chamber during the deformation.
$h, h_c, \Delta h$	**Chamber height** during the deformation, in the undeformed configuration, and the difference of height $\Delta h = h - h_c$.
$L_i, L_i^c, \Delta L_i, i \in [x, y, z], \alpha_y, \alpha_z$	**Dimensions of the chamber in the x, y, z directions** during the deformation, in the undeformed configuration, difference of length compared to the undeformed state. Ratios of deformations : $\alpha_y = \frac{\Delta L_y}{\Delta L_x}, \alpha_z = \frac{\Delta L_z}{\Delta L_x}$.

Supplementary references

1. Andersen JB, Sternberg C, Poulsen LK, Bjorn SP, Givskov M, Molin S. New unstable variants of green fluorescent protein for studies of transient gene expression in bacteria. *Appl Environ Microbiol* 64 (6), 2240-6 (1998).
2. Rollin R, Joanny JF, Sens P. Physical basis of the cell size scaling laws. *eLife*, 12:e82490 (2023).
3. Lemière J, Real-Calderon P, Holt LJ, Fai TG, Chang F. Control of nuclear size by osmotic forces in Schizosaccharomyces pombe. *eLife*, 11:e76075 (2022).
4. Deviri D, Safran SA. Balance of osmotic pressures determines the nuclear-to-cytoplasmic volume ratio of the cell. *PNAS*, 119(21):e2118301119 (2022).
5. Venkova L, Vishen AS, Lembo S, Srivastava N, Duchamp B, Ruppel A, Williart A, Vassilopoulos S, Deslys A, Garcia Arcos JM, Diz-Munoz A, Balland M, Joanny JF, Cuvelier D, Sens P, Piel M. A mechano-osmotic feedback couples cell volume to the rate of cell deformation. *eLife*, 11:e72381 (2022).
6. Campas O, Mahadevan L. Shape and Dynamics of Tip-Growing Cells. *Current Biology*, 19(24):2102–2107 (2009).
7. Park JO, Rubin SA, Xu YF, Amador-Noguez D, Fan J, Shlomi T, Rabinowitz JD. Metabolite concentrations, fluxes and free energies imply efficient enzyme usage. *Nature Chemical Biology*, 12(7):482–489 (2016).
8. Alric B, Formosa-Dague C, Dague E, Holt LJ, Delarue M. Macromolecular crowding limits growth under pressure. *Nature physics*, 18(4):411–416, (2022).
9. Schmoller KM, Turner JJ, Koivomagi M, Skotheim JM. Dilution of the cell cycle inhibitor Whi5 controls budding-yeast cell size. *Nature*, 526(7572):268–272 (2015).
10. Zatulovskiy E, Zhang S, Berenson DF, Topacio BR, Skotheim JM. Cell growth dilutes the cell cycle inhibitor Rb to trigger cell division. *Science*, 369(6502):466–471 (2020).
11. Si F, Le Treut G, Sauls JT, Vadia S, Levin PA, Jun S. Mechanistic Origin of Cell-Size Control and Homeostasis in Bacteria. *Current Biology*, 29(11):1760–1770.e7 (2019).
12. Milo R, Philipps R. *Cell Biology by the numbers*. 2015.